Proceedings World Geothermal Congress 2023
Beijing, China, April 17 – 21, 2023

Calibrating wellbore stress-strength models from borehole geometry and stress measurements

Andrés Alcolea, Asmae Dahrabou, Benoît Valley, Peter Meier, Philip Brunner

Geo-Energie Suisse AG, Reitergasse 11,8004, Zürich, Switzerland

a.alcolea@geo-energie.ch

Keywords: Borehole failure, Stress state-Strength models, Calibration, Enhanced geothermal system

ABSTRACT

Borehole stability is a major concern in the drilling and operational phases of a deep geothermal project. The shape and especially the direction of the borehole must be controlled during drilling to ensure (1) stability to avoid expensive losses of rig time, (2) a borehole trajectory intersecting enough structures (e.g., fractures or fault zones, initially not water conductive) for the posterior engineering of the reservoir, and (3) a sufficiently smooth borehole wall to facilitate borehole completion (e.g., the installation of packers/multi-packers for a multi-stage hydraulic stimulation). During the operational phase, the partial or total collapse of the borehole and the inflow/circulation of solid particles must be prevented to avoid damage to the injection/production pumps.

Borehole stability is controlled by the complex interactions between the state of stress and the strength of the surrounding rock. Thus, a proper characterization of these parameters together is crucial to the success of a deep geothermal project. The vertical and minimum horizontal principal stresses (S_v and S_{hmin}, respectively) can be inferred by integrating the density log and by interpreting, e.g., mini-frac tests respectively. Instead, the maximum principal stress, S_{Hmax} is difficult to constrain and, often, only rough estimates are obtained after imposing frictional equilibrium. In this work, we present a systematic methodology to jointly evaluate the non-linear heterogeneous distributions along the borehole profile, of (1) the full stress tensor, defined by the three principal stresses and corresponding orientations and, (2) the properties (e.g., cohesion, friction) defining the rock strength model. Model parameters are calibrated from measurements of borehole geometry acquired during or shortly after drilling (breakout width, extent/depth of failure, orientation and drilling induced tensile fractures). Additionally, prior estimates or direct measurements of model parameters can be incorporated in the calibration process. The parameter estimates, obtained via inverse problem, are non-unique, which leads to a broad range of equally plausible stress-strength solutions. We demonstrate that the inherent parametric uncertainties are drastically reduced by conditioning the model to hard measurements (e.g., S_{hmin} at a given depth interpreted from a XLOT). The calibrated model (or models) can be used for, e.g., determining the optimum trajectory of the deviated section of a borehole, or the optimum completion scheme.

For illustration purposes, the methodology is applied to the extensive data set along the crystalline section of borehole BS-1, in Basel (Switzerland). The methodology allows us (1) to derive plausible sets of stress and strength parameters matching the heterogeneous distribution of breakouts along BS-1 (including areas with the absence of breakouts), (2) to demonstrate the benefit of conditioning parameter estimates to direct measurements of calibration parameters, and (3) to unveil the paradox of having no borehole breakouts at sections of the borehole with high density of natural fractures.

1. INTRODUCTION

Drilling performance of deep Enhanced or Engineered Geothermal Systems (EGS) largely depends on borehole stability, which is controlled by the interplay between the local state of stress and the strength properties of the rock around the borehole. Borehole stability is crucial not only during drilling, but at any stage of maturity of the EGS. During completion, deeply penetrating borehole breakouts may entangle, and even preclude the correct placing of packers for zonal or multizonal isolation, thus forcing the use of expensive cased and cemented long borehole sections that must be perforated for establishing the connection between borehole and reservoir. During the operational phase, the partial or total collapse of an open section of the borehole, involving the likely circulation of solid particles, must be prevented to avoid damage to the production pump. For the aforementioned reasons, and regardless of the completion scheme, accurate knowledge of the interplays between stress and strength properties is crucial to the success of an EGS.

Due to the dominant effect of gravity, and given the small range of density variations in most rocks, one principal stress is usually taken as vertical and inferred by integrating the density log. This assumption may be inaccurate due to, e.g., topographic effects (Evans and Meier, 1995) or the presence of an excavation nearby (Martin et al., 2003) that may strongly decompress the rock and change the direction of the principal stresses, or by the drilling process itself (Kutter, 1991). Extended leak off tests (XLOTs, Lin et al., 2008) or mini-frac tests (Bröker and Ma, 2022) are often used to estimate the minimum principal stress (S_{hmin} in normal and strike-slip faulting environments and S_v in reverse faulting environments) at the test depth only, which becomes expensive at typical depths of an EGS. The direction of the maximum extent of borehole breakouts is usually an accurate estimate of the orientation of the maximum principal stress (S_{Hmax} in vertical boreholes; Zoback et al., 2003). However, the magnitude of the maximum principal stress is difficult to constrain and, often, rough estimates are inferred by imposing frictional equilibrium (Zoback, 2007), which assumes a certain (but very uncertain) strength model. As such, deciding a completion scheme, or the trajectory of a branch of a deviated borehole, is most often made on costly and uncertain estimates of the local stress tensor based on weak assumptions at one single point at best.

This work is aimed at filling this gap. We propose a workflow for the joint estimation of stress and strength profiles along the borehole based on (1) borehole geometry (radius, azimuth and deviation), (2) borehole breakouts (width, extent/depth of failure and orientation), (3) the presence/absence of drilling induced axial or en-echelon tensile fractures (A-DITFs and E-DITFs, respectively),

(4) measured mud density, and (5) prior point estimates or measurements of stress and strength parameters (e.g., S_3 from XLOTs or mini-frac field tests, or the Uniaxial Compressive Strength measured in the laboratory, etc.). The estimated profiles can be linear (so-called first order estimate depicting depth-trends) or not (second order estimate depicting the variation of a given parameter about the first order trend). In addition, the borehole can be segmented, representing different strata with corresponding different stress and strength models. Model parameters are estimated by the Regularized Pilot Points Method (Doherty, 2003; Alcolea et al., 2006), as implemented in PEST (Parameter ESTimation; Doherty, 2015) and considering the Kirsch (1898) analytical solution as fast forward simulator and a modified version of Shen's formula (Shen, 2008). The main outputs of the workflow are first or second order borehole profiles of (1) the magnitudes of the three principal stresses, (2) the corresponding orientations, depicted by the three Euler angles, (3) the remnant thermal stresses caused by the cooling of the borehole wall, (4) the parameters defining the strength model (formulation, i.e., Mohr-Coulomb or Mogi-Coulomb so far, cohesion and friction), and (5) the parameters governing Shen's formula. The workflow, presented in detail in Dahrabou et al. (2022), is summarized and applied to assess the variability of stress and strength along the 2.5 km crystalline section of the BS-1 borehole in Basel (Switzerland; Häring et al., 2008).

2. WORKFLOW

The workflow follows roughly the five consecutive steps sketched in Figure 1:

- Step 1: given a set of initial parameters (e.g., slope of the depth trends of S_1, Young's modulus, thermo-elastic parameters, etc.), calculate stresses around the borehole using Kirsch closed-form solution (Kirsch, 1898).
- Step 2: evaluate failure conditions. So far, Mohr–Coulomb and Mogi–Coulomb criteria have been implemented. Nonetheless, any other failure criterion can be implemented without loss of generality.
- Step 3: evaluate breakout width, extent and orientation, and the presence of DITFs.
- Step 4: evaluate a penalty function (so-called objective function) measuring the departure of the obtained solution from available measurements. Measurements include geometric features (i.e., borehole shape and presence/absence of DITFs), prior estimates of unknown parameters or direct parameter measurements at certain depths.
- Step 5: modify parameters and go back to Step 1, until a minimum of the objective function is attained. This step is the so-called parameter estimation, optimization or, in a broad sense, inverse problem (Carrera et al., 2005). The aforementioned workflow is carried out by the generic parameter estimation software PEST (Doherty, 2015).

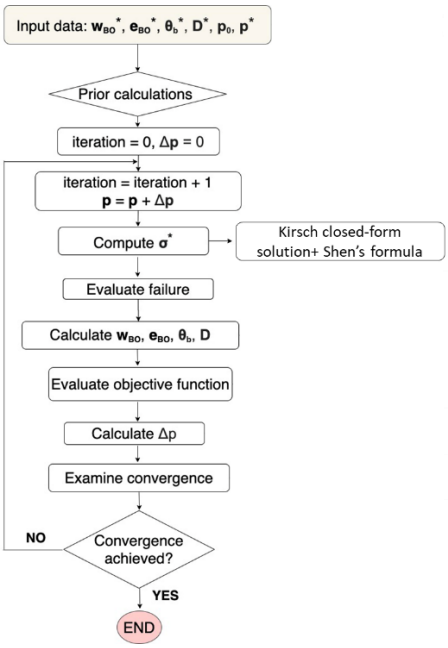

Figure 1: Schematic description of the proposed methodology. In the insets, $\boldsymbol{p_0}$ and $\boldsymbol{p}$ are the initial and sequentially updated sets of parameters, respectively; $\boldsymbol{w}$, $\boldsymbol{e}$ and $\boldsymbol{\theta}$ are vectors containing calculated breakout width, extent/depth of failure and orientation; vector $\boldsymbol{D}$ represents the presence or absence of DITFs; the corresponding magnitudes with asterisk represent the measured counterparts. Modified from Dahrabou et al., 2022.

2.1 Calculation of stresses

We have chosen a Kirsch elastic analytical solution because it is (1) well established as standard practice in borehole design, (2) computationally faster than, e.g., numerical models, and (3) easy to implement. Dahrabou et al. (2022) discuss the limitations of the analytical solution. Nonetheless, the closed-form solution, implemented as a black-box in the workflow, can be replaced by a more sophisticated forward simulator if more accuracy is needed, e.g., to evaluate the temporal evolution of breakout extent after drilling. Our current implementation accounts for boreholes not parallel to one of the principal stresses and includes a thermos-elastic stress component to simulate remnant thermal stresses caused by the cooling of the borehole wall.

The total stresses (arranged in a tensor $\boldsymbol{S}$) around a borehole of radius a, in cylindrical (borehole) coordinates (r, θ, w), filled with an internal fluid (mud) at a pressure P_m, and subject to thermal stresses are:

$$
\begin{aligned}
S_{rr} &= \left(1-\frac{a^2}{r^2}\right)\left(\frac{S_u+S_v}{2}\right)+\left(1+\frac{3a^4}{r^4}-\frac{4a^2}{r^2}\right)\left(\frac{S_u-S_v}{2}\right)cos2\theta \\
&\quad +\left(1+\frac{3a^4}{r^4}-\frac{4a^2}{r^2}\right)S_{uw}sin2\theta+P_m\left(\frac{a^2}{r^2}\right) \\
S_{\theta\theta} &= \left(1+\frac{a^2}{r^2}\right)\left(\frac{S_u+S_v}{2}\right)-\left(1+\frac{3a^4}{r^4}\right)\left(\frac{S_u-S_v}{2}\right)cos2\theta-\left(1+\frac{3a^4}{r^4}\right)S_{uw}sin2\theta-P_m\left(\frac{a^2}{r^2}\right) \\
&\quad +\frac{\beta E\Delta T}{1-\nu} \\
S_{ww} &= S_z-4\nu\frac{a^2}{r^2}\left(\frac{S_u-S_v}{2}\right)cos2\theta-4\nu\frac{a^2}{r^2}S_{uv}sin2\theta+\frac{\beta E\Delta T}{1-\nu} \\
S_{r\theta} &= -\left(1-\frac{3a^4}{r^4}+\frac{2a^2}{r^2}\right)\left(\frac{S_u-S_v}{2}\right)sin2\theta+\left(1-\frac{3a^4}{r^4}+\frac{2a^2}{r^2}\right)S_{uv}cos2\theta \\
S_{rw} &= \left(1-\frac{a^2}{r^2}\right)(S_{vw}sin\theta+S_{uw}cos\theta) \\
S_{\theta w} &= \left(1+\frac{a^2}{r^2}\right)(S_{vw}cos\theta-S_{uw}sin\theta)
\end{aligned}
\tag{1}
$$

where E and ν are the Young's modulus and the Poisson ratio, respectively, β is the coefficient of linear expansion and ΔT is the deviation from ambient temperature (i.e., internal minus external temperatures). Failure is checked in terms of the effective stress tensor $\boldsymbol{\sigma}$:

$$
\sigma = \boldsymbol{S}-\gamma\,\delta_{ij}P_p\left(\frac{a^2}{r^2}\right) \tag{2}
$$

where P_p is pore pressure, γ is the effective stress law coefficient (Biot, 1941 and 1955; Biot and Willis, 1957) and δ_{ij} is the Kronecker δ that applies Terzaghi's correction to diagonal components of $\boldsymbol{S}$ only.

2.2 Strength models

An important issue in the analysis of wellbore stability is the selection of an appropriate rock failure criterion. Without loss of generality, we focus here on the Mohr–Coulomb criterion because it is the most used in practice. Dahrabou et al. (2022) also explored the Mogi–Coulomb criterion. The Mohr–Coulomb criterion assumes that σ_2 has no influence on rock strength, and is expressed in terms of principal stresses as:

$$
\begin{aligned}
\sigma_1 &= C_0+q\sigma_3 \\
q &= tan\left(\frac{\pi}{4}+\frac{\psi}{2}\right)^2 \\
C_0 &= \frac{2ccos\psi}{1-sin\psi}
\end{aligned}
\tag{3}
$$

where C_0 is the uniaxial compressive strength of the rock, and q is a material constant, both related to the internal friction angle, ψ, and the cohesion, c.

Regardless of their formulation, failure criteria are difficult to parameterize. Both friction and cohesion can be measured in the laboratory. Unfortunately, this is rarely the case in practice because (1) retrieving cores from deep boreholes is expensive and time-consuming, and (2) laboratory conditions rarely represent in-situ conditions due to scale effects. A possible simplification is to set the cohesion to zero because that represents the worst-case scenario (i.e., closest to failure). However, the cohesion of crystalline rocks can be large (e.g., in Basel, cohesion ranges from 18.2 MPa to 35.5 MPa; Valley and Evans, 2019). To make things worse, uncertainties become critical in what concerns friction. Typically, the friction coefficient is set to 0.6, value qualified as that of the critically stressed crust (Barton, 1976). Such value has been criticized by many authors on the basis of experimental data. For instance, laboratory analysis in the context of the Pohang EGS report values ~1.7 for an intact granite (Kwon et al., 2019). Instead, Alcolea et al. (2020) report low values in the range 0.4–0.45 for a fault zone in the same crystalline formation. Barton (1974) and Hoek (2007) provide comprehensive databases of friction coefficients for different filled discontinuities and filling materials. We consider the uncertainties inherent to strength parameters by means of model calibration (See Section 2.5).

2.3 Estimation of breakout geometry

Breakout geometry is fully defined by its width, *w*, its extent, *e*, and the angle of maximum extent, θ. Breakout width is calculated after checking failure at the borehole wall using equations 1 to 3. The arc, measured as angle, along which the failure criterion is met provides an estimate of *w*. Here, we assume that the initial failure width is maximum and instantaneous, i.e., breakouts are generated but only deepen and not widen. Although some modifications of breakout width with time have been reported in-situ (Azzola et al., 2019), the approach implemented in our methodology is widely accepted (Zoback et al., 2003).

Approaches to compute breakout extent, *e*, are scarce in the literature, possibly because breakout width has been traditionally chosen to estimate the state of stress. However, we argue that properly characterizing breakout extent is crucial, e.g., to guarantee proper packer sealing in the completion of multi-stage EGS stimulation. Unfortunately, the application of the same general principle as for the computation of breakout width, i.e., evaluating the failure criteria for $r > a$ using the Kirsch solution is not meaningful because progressive failure is neglected. An empirical and computationally affordable criterion is proposed by Shen (2008):

$$\frac{3\sigma_{Hmax}-\sigma_{hmax}}{C_0} = 1 + A\left(\frac{e}{a}-1\right)^B \tag{4}$$

where $\frac{3\sigma_{Hmax}-\sigma_{hmax}}{C_0}$ represents the ratio of the maximum effective tangent stress to the uniaxial compressive strength. A and B are calibration parameters. The strength is defined as a Rankine criterion, i.e., the minimum and intermediate principal stresses are ignored, which neglects the important stabilizing effect of the internal wellbore pressure (mud pressure). In our analyses, we extend Shen's criterion by defining an apparent wellbore strength σ_{app}, which for the Mohr–Coulomb failure criterion becomes:

$$\sigma_{app} = q\,\sigma_3 + C_0 \tag{5}$$

Once the apparent strength has been determined, the breakout extent is evaluated using equation (4) and replacing $\frac{3\sigma_{Hmax}-\sigma_{hmax}}{C_0}$ by $\frac{\sigma_1}{\sigma_{app}}$, where σ_1 is the maximum effective stress at the breakout centre point (i.e., the direction of maximum breakout extent).

2.4 Estimation of DITFs occurrence

The occurrence of drilling induced tensile fracture is evaluated by the Rankine criterion:

$$\sigma_3 \leq T_0 \tag{6}$$

where T_0 is the tensile strength (negative meaning tension). Note that both axial and en-echelon tensile fractures, A-DITFs and E-DITFs (Brudy and Zoback, 1993) are considered jointly in our implementation.

2.5 Estimation of model parameters

The parameterization depends on the desired characterization. First order characterization aims at estimating depth trends. In such case, a generic parameter *p* is expressed generically as:

$$p = a \cdot TVD + b \tag{7}$$

Second order characterization aims at estimating the deviations of a given parameter from its estimated trend (i.e., the first order characterization), which enables the analysis of variability at all scales. A generic parameter *p* now becomes

$$p = a \cdot TVD + b + \varepsilon(MD) \tag{8}$$

where ε is the perturbation of the parameter around its trend and depends on measured depth (*MD*) to account for deviated boreholes. Note that, instead, the general expression of a parameter depends on true vertical depth (*TVD*) because most of them are expressed as a vertical depth gradient. Indeed, both *TVD* and *MD* are mapped univocally through the measured borehole trajectory.

The main strength of our methodology is the joint calibration of the stress and strength models. Commonly, parameter uncertainties are taken into account through parametric sensitivity analysis or manual trial-and-error calibration at best. Instead, we cast the estimation problem in the mathematical framework of automatic inverse modelling. In broad terms, inverse modelling refers to the process of gathering information about the model from measurements of what is being modelled (Carrera et al., 2005). Once a conceptual model is represented by equations (Sections 2.1 to 2.4), the inverse problem consists of estimating the plausible set (or sets) of parameters that best fit observations through the aforementioned mapping equations. This is achieved by minimizing a penalty function *F*, so-called objective function, which measures the misfit between calculated and observed values, arranged in vectors $\boldsymbol{\Theta}$ and $\boldsymbol{\Theta}^*$, respectively, with components $\boldsymbol{\Theta} = \{\boldsymbol{w}, \boldsymbol{e}, \boldsymbol{\theta}, \boldsymbol{D}\}$ representing subsets of breakout width, extent and orientation and drilling induced tensile fractures. The set of calibrated parameters, described below, is arranged in vector $\boldsymbol{M}$, with corresponding prior estimates arranged in vector $\boldsymbol{M}^*$. The objective function *F* can be expressed in a generic manner as

$$F = \sum_{i=1}^{4} \lambda_i (\Theta_i - \Theta_i^*)^t \boldsymbol{V}_i^{-1} (\Theta_i - \Theta_i^*) + \sum_{j=1}^{npar} \beta_j \left(\boldsymbol{M}_j - \boldsymbol{M}_j^*\right)^t \boldsymbol{V}_j^{-1} \left(\boldsymbol{M}_{ji} - \boldsymbol{M}_j^*\right) \tag{9}$$

where subscripts *i* and *j* refer to the type of measurement (*i*=1 for breakout width, *i*=2 for extent, etc.) and parameter, (j=1 for parameters characterizing stress, j=2 for parameters characterizing strength, etc). The scalars λ_i and β_j represent global weights balancing the contribution of the individual pieces of information. Matrices $\boldsymbol{V}_i$ and $\boldsymbol{V}_j$ are the prior covariance matrices including the inherent uncertainty of each measurement/parameter prior estimate and the possible correlations between them. Note that equation 7 is that of generalized least squares method or of the maximum likelihood information including prior information of model parameters (Edwards, 1974). The first term in F accounts for the misfit between calculated and observed breakout geometries and drilling-induced tensile fractures, whereas the second term, so-called plausibility term, penalizes the departures between parameters and the corresponding prior information arising, e.g., from laboratory tests and/or field tests like XLOTs. Thus, we aim at finding not only the typically display "goodness of fit", but to achieve it with plausible parameters. Regardless of the characterization (first order or second order), model parameters are estimated by the Regularized Pilot Points Method (RPPM, Alcolea et al., 2006), as implemented in the free Parameter ESTimation software, PEST (Doherty, 2015).

3. DESCRIPTION OF BS-1 DATA

The vertical borehole BS-1 was drilled to a depth of 5 km in the crystalline basement in 2006 in Basel (Switzerland), as part of an intended Enhanced Geothermal System (EGS). Ultrasonic borehole televiewer (UBI) logs were run from 2578 to the bottom hole shortly after drilling. A detailed description of the Basel EGS and of the BS-1 borehole is available in Häring et al. (2008), amongst others. The borehole data used in our analysis and the procedure to infer borehole failure are described in detail in Valley and Evans (2009 and 2019).

Borehole breakouts were identified along 81% of the total length of the logged section and are almost continuous except for a large gap from 2747 m TVD to 2899 m TVD and some other minor gaps at 3820–3856 m TVD, 4185–4221 m TVD and 4582–4631 m TVD (Figure 2). The aforementioned borehole segments coincide with those of strong intensity of natural fractures. This paradox, involving the presence of natural fractures but the absence of borehole breakouts, occurs frequently in deep boreholes and is attributed to local heterogeneities of rock stiffness, i.e., fractures softening the rock mass thus leading to less breakouts (Dahrabou et al., 2022). Borehole geometry was averaged from the inferred breakouts at cross sections with a longitudinal spacing of 40 cm (5001 sections for each type of measurements, and, overall, 20004 sections). Instead, DITFs are present in 20% of the logged section only.

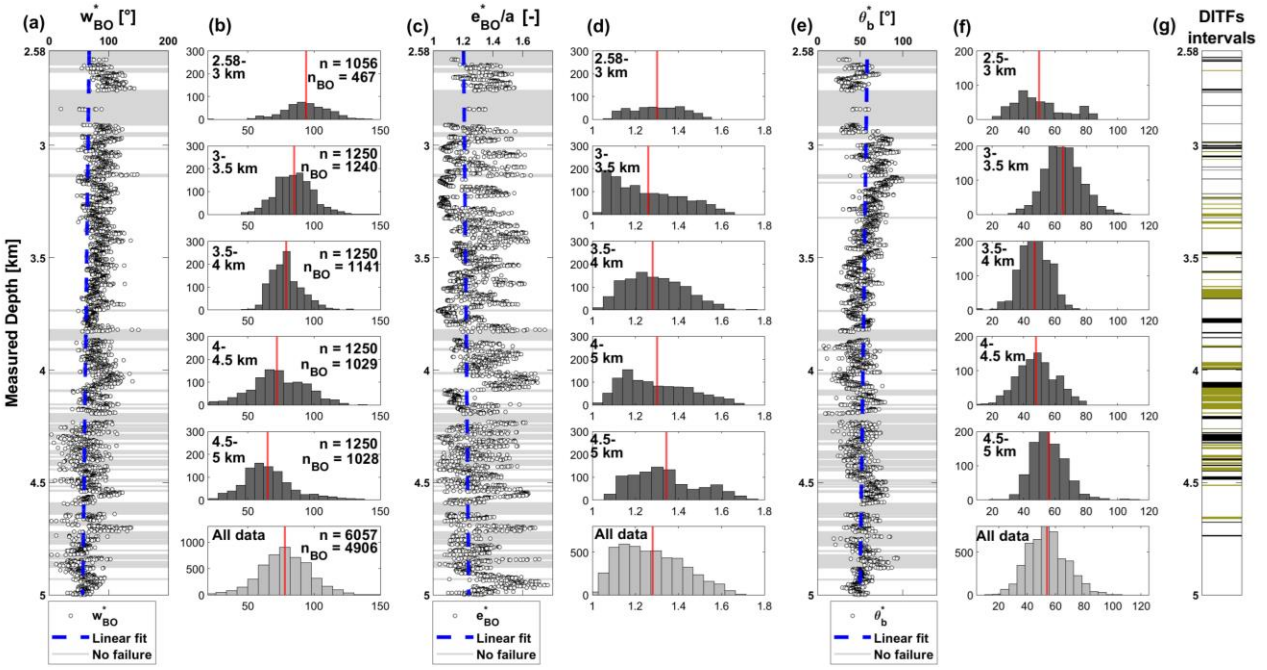

Figure 2: Interpreted failure data along borehole BS-1: (a, c and e) Spatial distribution of breakout width (ω_{BO}), extent normalized by borehole radius (e_{BO}/a) and orientation (θ_b), respectively. The dashed lines represent linear depth trends and the horizontal grey shaded zones represent cross-sections without breakouts; (b, d and f) histograms of the aforementioned magnitudes along 500 m long borehole sections and considered altogether (panels on bottom). The insets report on the number of sections (n) and the number of sections where breakouts occur (n_{BO}). The red lines depict mean values; (g) Observed DITFs intervals (green = en-echelon; black = axial). Source: Modified from Valley and Evans (2009).

A number of prior analyses, based on borehole geometry analyses (Valley and Evans, 2009 and 2019), on focal mechanisms (Deichmann and Giardini, 2009; Kastrup et al., 2004; Kraft and Deichmann, 2014; Terakawa et al., 2012), or on numerical simulations (Häring et al., 2008) provide prior information on the local stress regime. These are summarized in Figure 3. As is often the case in practice, stress estimates attained using different methods and sources lead to unalike results. The main discrepancies between prior studies concern the S_{hmin} and S_{Hmax} profiles. The profiles proposed by Valley and Evans (2019) share the commonality of a very low stress gradient required to explain the fact that breakout width decreases with depth while assuming that the borehole wall strength remains constant, as supported by the homogeneity of the rock along the BS-1 basement section. The absolute value of S_{Hmax} is highly uncertain because it depends strongly on the chosen failure criterion and its parameterization, for which there is no robust evidence. The focal mechanisms of induced seismic events indicate a mix of strike-slip and normal faulting regimes at the level of the reservoir. The stress profiles proposed by Valley and Evans (2019) are consistent with this observation. All proposed profiles are also consistent with the limits imposed by the frictional strength of the earth crust (Zoback et al., 2003).

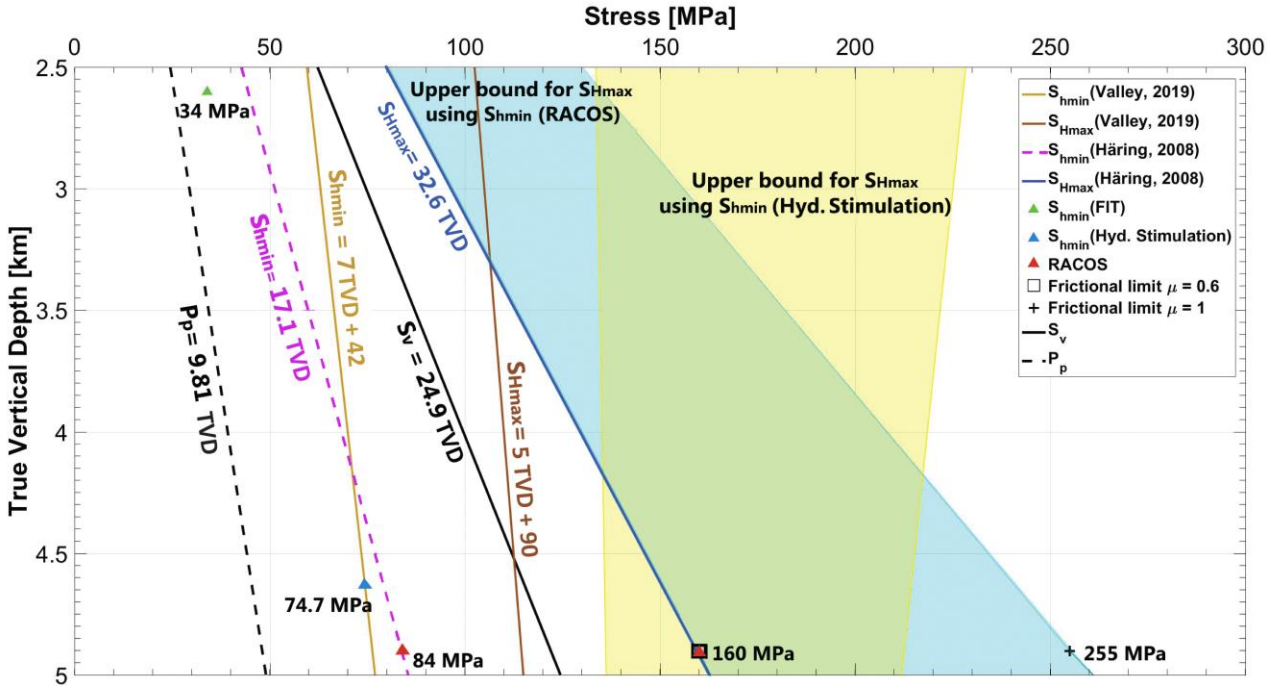

Figure 3: Constraints on S_{hmin} and S_{Hmax} in the BS-1 well inferred from hydraulic data, FIT test and RACOS (Braun, 2007) as compiled by Häring et al. (2008). Profiles of S_{Hmax} and S_{hmin} from Valley and Evans (2019) are also presented. The coloured areas depict upper bounds for S_{Hmax} considering frictional equilibrium (Zoback, 2007), friction coefficients between 0.6 and 1.0 and the two proposed profiles of S_{hmin}. The orientation of S_{Hmax} is common to all analyses, i.e., 144 ± 14° (Valley and Evans, 2009).

4. CALIBRATION OF THE DEVELOPED GEOMECHANICAL MODEL

Measurements of the deepest section of the borehole (3 to km depth) were used to calibrate model parameters defining the first order (i.e., linear trends with depth) and second order (deviations from the trend) characterizations. The following assumptions are made:

- The vertical stress, S_v, is principal and known, which reduces the number of model parameters. This is justified by the observed small deviations of the density log around its linear depth trend and is attributed to the homogeneity of the crystalline section of the BS-1 borehole observed in the cuttings retrieved during drilling.
- In the same line of arguments, the azimuth of the maximum principal stress S_{Hmax} and the strength parameters (internal friction angle, ψ, cohesion c, and modified Shen's parameters A and B) are considered constant in the first order approach. Nonetheless, our methodology is generic and linear depth trends can be accommodated for any of the aforementioned parameters.
- The parameters controlling thermal stresses, E and ν, are assumed constant and known. They are usually inferred after the dynamic to static correction of the sonic log in the best case, or inherited from existing literature in most cases. The impact of stiffness variations is discussed in Dahrabou et al. (2022).
- In the absence of further information, the distribution of formation pressure is assumed to be hydrostatic, which further reduces the parameterization. Although for example at the BS1 site, slightly artesian conditions were encountered, we argue that deviations from the hydrostatic distribution are small compared to uncertainties on other model parameters.

The first order parameterization is summarized in vector $\boldsymbol{M}$ (equation 22) and includes the definition of the linear trends of S_{Hmax} and S_{hmin}, the azimuth of S_{Hmax} (first Euler angle α), the strength parameters defining the Mohr-Coulomb criterion (cohesion c and internal friction angle Ψ), and the parameters A and B defining the modified Shen's formulations:

$$\boldsymbol{M} = \left\{a_{S_{Hmax}}, b_{S_{Hmax}}, a_{S_{hmin}}, b_{S_{hmin}}, \alpha, c, \Psi, A, B\right\} \tag{10}$$

The second order characterization is carried out by estimating (1) $\boldsymbol{M}$, and (2) perturbations about the trend values at so-called pilot points, regularly spaced every 10m (overall 1407 pilot points).

4.1 First order characterization

A number of starting points is used in the calibration to guarantee that a global optimum is achieved by the Levenberg–Marquardt algorithm (Alcolea et al., 2000). To that end, the prior distribution of each parameter, defined by plausible upper and lower bounds out of literature or from previous studies, is randomly sampled assuming a uniform distribution, which renders overall 200 initial parameterizations that explore the global parameter space. An initial rejection criterion, based on frictional equilibrium, is applied to the initial starting points by checking coherency and frictional equilibrium, i.e., $S_{Hmax} > S_{hmin}$ and $\frac{S_1 - P_p}{S_3 - P_p} \leq \left[\sqrt{\mu^2 + 1} + \mu\right]^2$, where S_1

and S_3 are the maximum and the minimum total principal stresses respectively, P_p is pore pressure and μ is friction coefficient, i.e., $\mu = \tan(\Psi)$.

Initial sets of parameters not meeting the aforementioned constraints are rejected and new ones are generated until the target 200 initial coherent parameterizations is achieved. Note that initial sets of parameters may lead to different final optimum sets of calibrated parameters with similar final values of the objective function F. This is a common issue in inverse problem theory, known as non-uniqueness (Carrera and Neuman, 1982; Carrera et al., 2005). Assumptions are required for model parameters that are not calibrated. We use the following linear trends (on True Vertical Depth, TVD) of S_v and P_p:

$$S_v\ [\text{MPa}] = 24.9 \cdot \text{TVD}[\text{km}]$$
$$P_p\ [\text{MPa}] = 9.81 \cdot \text{TVD}[\text{km}] \quad (11)$$

Based on the mud density measurements collected during the drilling of BS-1, we assume a hydrostatic mud pressure corresponding to an equivalent mud density, ρ_m = 1.07 g/cm3. We use the actual BS-1 borehole trajectory in our computations. Different cooling profiles for breakouts and DITFs after Valley and Evans (2019) were used to estimate thermal stresses, the Young's modulus (E = 65 GPa) and the coefficient of linear expansion ($\beta = 10^{-5}$ K^{-1}). In addition, a set of bounding thresholds is implemented in PEST to minimize unwanted and large parameter oscillations.

A posterior rejection criterion was defined by setting a maximum threshold for the objective function after calibration, and calibrated models with the final objective function above the threshold were rejected. After this rejection process, only 136 calibrated models were kept. Figure 4 shows calculated failure observations and the accepted calibrated horizontal principal stresses. As observed, breakout width tends to decrease with depth while breakout extent does not vary much, which is consistent with the BS-1 borehole observations in Figure 2. This can be explained by the low slopes of calibrated stresses (a_{SHmax} and a_{Shmin}, with mean values 4.3 and 7.2 MPa/km, respectively), which resemble well the experimental results in Valley and Evans (2019). All models converge towards a breakout orientation θ_b = 54°, which is precisely the orientation of S_{hmin} reported in Valley and Evans (2019). The non-uniqueness of the solution is illustrated by the wide envelopes of calculated stress profiles (in red and blue in Figure 4).

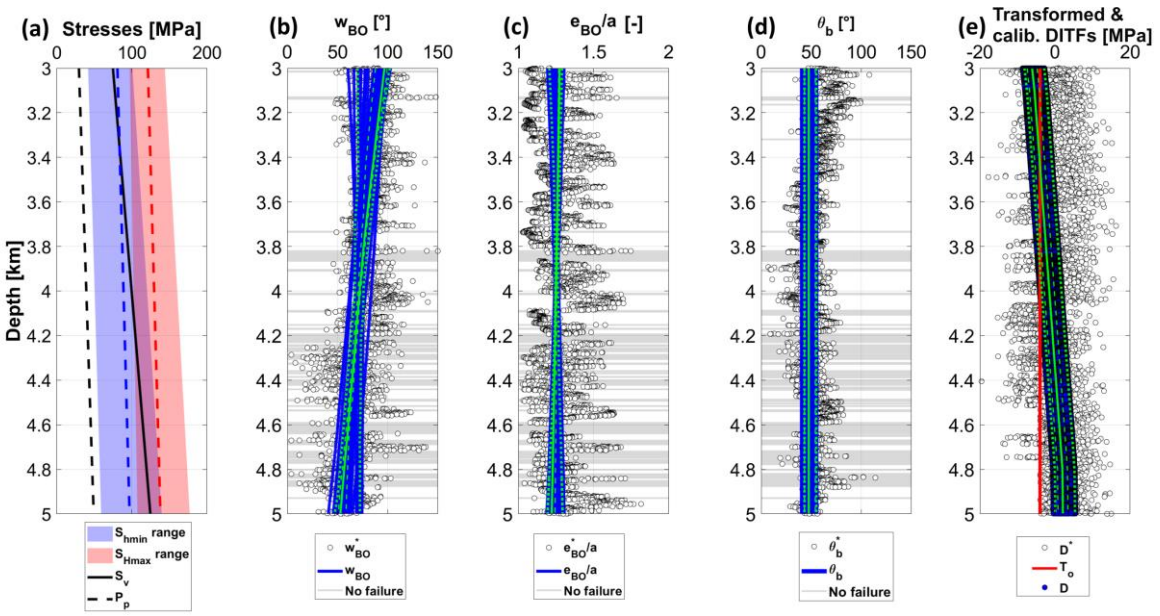

Figure 4: First order calibration results. (a) range of the calibrated S_{Hmax} (shaded in red) and S_{hmin} (shaded in blue) for 136 accepted models. S_v and P_p profiles are depicted by the solid and dashed black lines, respectively. The blue and red dashed lines depict the mean of the ranges of the calibrated S_{hmin} and S_{Hmax}, respectively; (b) calibrated and measured breakout width; (c) normalized breakout extent; (d) breakout orientation; (e) DITFs. In panels (b) to (d), the black symbols depict measurements, whereas in panel (e), they depict the estimated minimum hoop stress derived from DITFs observations. In panels (b) to (e), the blue lines represent the outputs of the calibrated models. The grey shaded zones represent depth ranges without breakouts. The red line in panel (e) corresponds to tensile strength, $T_o = -4$ MPa. Finally, the solid green lines correspond to the mean of the outputs of the 136 accepted models, whereas the dashed lines represent the 25th–75th and 5th–95th percentiles.

Non-uniqueness is efficiently tackled by adding hard measurements of estimated parameters. In this case, the best estimate of S_{hmin} in Häring et al. (2008) is added as conditioning measurement at a depth of 4632m MD. Alternatively, stress measurements inferred from XLOTs (Lin et al., 2008) can be added as conditioning measurements. Notably, on-going applied research is devoted to the direct inference of stresses from deformations measured during hydraulic fracturing tests or during hydraulic stimulation of pre-existing fractures (the SPINE project, http://www.geothermica.eu/projects/call-2/spine/; Williams et al., 2022; Zabihian et al., 2022). The first order characterization was repeated using the same 200 set of initial values. After applying the rejection criterion, only 120

calibrated models were retained. Figure 5 shows show the dramatic reduction of uncertainty in the calibrated stress model, as displayed by the narrower envelopes of plausible solutions.

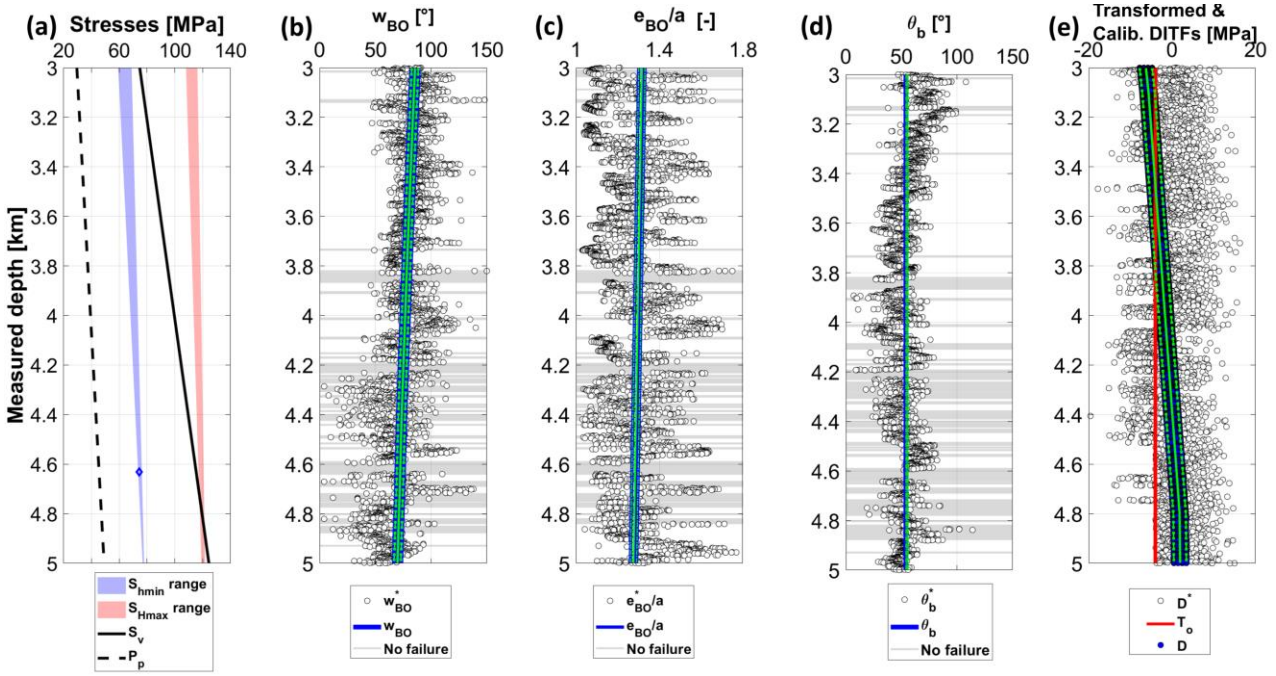

Figure 5: First order characterization in the presence of a new measurement of S_{hmin}. See the caption of Figure 4 for further details.

4.2 Second order characterization

The first order calibration presented so far yields practical insights into the general trends of both stress and strength along the borehole. While trends are representative of the mean conditions along the borehole, they do not capture potentially large local variations that may cause completion problems (e.g., selection of packer sits). To fill this gap, the second order calibration is carried out using as starting parameterization and prior information the first order parameter values leading to the median profile of S_{Hmax} in Figure 4. Only one calibration is presented here for the sake of brevity. Each parameter in vector intervening in model equations is now parameterized with pilot points regularly spaced every 10 m. The pilot point discretization is common to all strength and stress parameter profiles, which leads to an overall parameterization involving 1407 pilot points. Ordinary kriging was used as spatial interpolation algorithm to render continuous profiles from values at pilot points.

The results in terms of goodness of fit and derived parameters are displayed in Figure 6 and Figure 7, respectively. The second order calibrated outputs (Figure 6) resemble not only the trends observed in measurements, but also the corresponding small-scale variabilities. The goodness of fit is striking, the root mean square errors being 10°, 0.086, 9° and 4.6 MPa for breakout width, normalized extent, orientation and DITFs, respectively (the initial misfits corresponding to the first order calibration were 27°, 0.175, 25° and 11.5 MPa). The second order calibrated outputs reproduce well most of the small gaps without breakouts (shaded blue areas in Figure 6a) and most of the maxima/minima of normalized extent (Figure 6b). The extreme values along measured profiles are not exactly captured because (1) the number of pilot points, which exerts major control on computation effort, is not enough for that purpose, and (2) capturing the variability at the smallest scale would lead to undesired large (although perhaps realistic) oscillations in the profiles of calibrated parameters in Figure 7. The derived parameters stress/strength in Figure 7 are all plausible. The stress profiles of S_{Hmax} and S_{hmin} reproduce well the transitional regime at ca. 4800 m depth reported by Valley and Evans (2019). The profiles of strength parameters in panels b to d display values coherent with those in the literature (also in Valley and Evans, 2019). It is worth noting how the interplay between stress and strength is properly captured by the second order characterization, i.e., there is a general negative correlation between the peaks of stress and strength at the gaps in the absence of breakouts (low stress/high strength or vice versa). The orientation of breakouts displays low departures (± 5°) from the median value of 144°, as reported in Häring et al. (2008). Finally, Shen's parameters defining the failure model are well within standard limits (Shen, 2008).

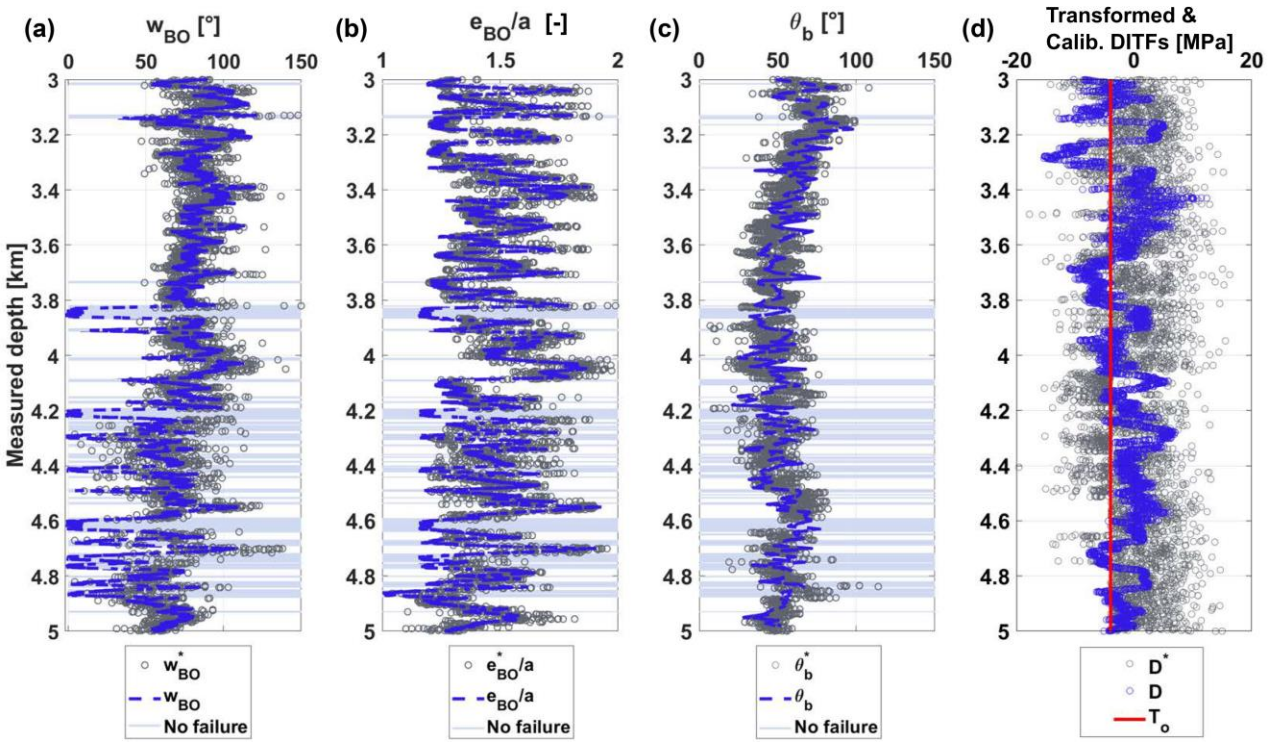

Figure 6: Second order characterization. (a) breakout width; (b) breakout extent; (c) breakout orientation; (d) Transformed and calibrated DITFs. In (a)–(c), the grey circles correspond to failure observations while in (e) they depict the estimated minimum hoop stress derived from DITFs observations. Light blue shaded areas in panels (a), (b) and (c) correspond to depths with no breakouts. The red line in panel (d) depicts the tensile strength, T_0= −4 MPa.

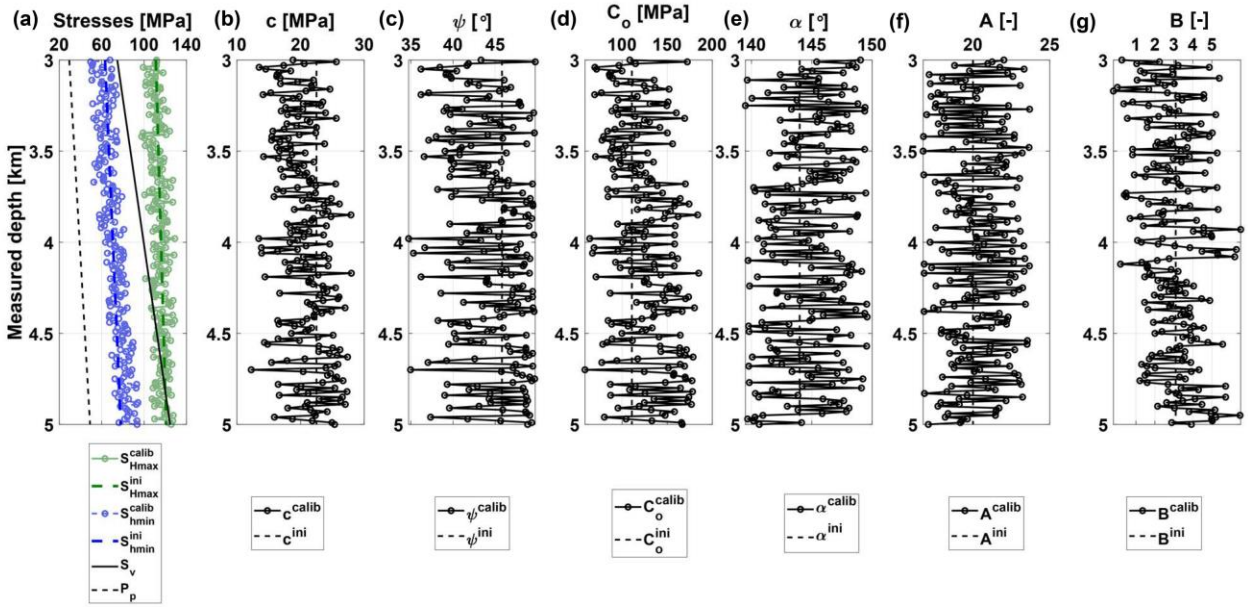

Figure 7: Second order characterization. (a) minimum and maximum principal horizontal stresses S_{Hmax} and S_{hmin}; (b) cohesion; (c) internal friction angle; (d) uniaxial compressive strength; (e) the angle α of Euler and the regression parameters of the modified Shen's formulation (f) *A* and (g) *B*. The dashed lines in all panels correspond to the initial depth profiles.

5. CONCLUSIONS

We propose a methodology to jointly evaluate the stress tensor components and orientations, and the rock strength properties (e.g., cohesion, friction) in a robust probabilistic framework. For this purpose, analytical and empirical solutions for estimating wellbore stresses and failure parameters are combined with the regularized pilot points method as implemented in the PEST software. We used measurements available during or shortly after drilling, i.e., breakout width, breakout extent and breakout orientation at different depths in addition to the presence/absence of DITFs (including both axial and en-echelon tensile fractures, A-DITFs and E-DITFs).

In addition, measurements of estimated parameters can be easily included in a generic manner (e.g., S_{hmin} interpreted from XLOT, or characterizations of the full stress tensor after SIMFIP measurements, Guglielmi et al., 2022). In fact, adding anchor points to the calibrated stress profiles is an efficient way to tackle non-uniqueness of the associated inverse problem. Also, all stress components around the borehole, including the remnant thermal stresses arising from the cooling of the borehole wall were accounted for. For illustration purposes, the proposed methodology was applied to the extensive borehole data set along the 2.5 km crystalline section of the borehole BS-1, in Basel (Switzerland). Our failure analyses approach and its application to the data set from the BS-1 borehole allow us to improve our understanding of failure processes in boreholes, the relationship amongst failure parameters and to better understand the stress and strength conditions and their variability in the earth crust.

ACKNOWLEDGMENTS

This work has been carried out with the framework of the SPINE (Stress Profiling in EGS) project. SPINE is subsidised through the Cofund GEOTHERMICA, which is supported by the European Union's HORIZON 2020 programme for research, technological development and demonstration, and benefits from an exploration subsidy of the Swiss federal office of energy for the EGS geothermal project in Haute-Sorne, canton of Jura (contract number MF-021-GEO-ERK), which is gratefully acknowledged.

REFERENCES

Alcolea, A., Ramírez, J., and Medina, A.: Pilot points method incorporating prior information for solving the groundwater flow inverse problem. *Advances in Water Resources*, **29**, (2006), 678–1689.

Alcolea, A., Meier, P., Vilarrasa, V., Olivella, S., and Carrera, J.: Induced seismicity assessment of the hydraulic stimulations in borehole PX2 at Pohang (South Korea) using coupled hydromechanical modelling. *Proceedings*, World geothermal congress 2020, Reykjavik, Iceland, (2020).

Azzola, J., Valley, B., Schmittbuhl, J., Genter, A.: Stress characterization and temporal evolution of borehole failure at the Rittershoffen geothermal project, *Solid Earth*, **10(4)**, (2019), 1155–1180.

Barton, N.R.: A review of the shear strength of filled discontinuities in rock, Norwegian Geotech. Inst. Publ. No. 105. Oslo, 1974.

Barton, N.: The shear strength of rock and rock joints, *International Journal of Rock Mechanics and Mining Sciences*, **13**, (1976),255–279.

Biot, M.: General theory of three-dimensional consolidation. *Journal of Applied Physics*,**12(2)**, (1941),155–164.

Biot, M.: The theory of elasticity and consolidation for a porous anisotropic solid. *Journal of Applied Physics*,**26**, (1955),182–185.

Biot, M. and Willis, D.: The elastic coefficients of the theory of consolidation. *Journal of Applied Mechanics*, **24**, (1957), 594–601.

Braun, R.: Analyse Gebirgsmechanischer Versagenszustände Beim Geothermieprojekt Basel. Report to Geopower Basel AG for Swiss Deep Heat Mining Project Basel, Basel, Switzerland, (2007)

Bröker, K., and Ma, X. Estimating the Least Principal Stress in a Granitic Rock Mass: Systematic Mini-Frac Tests and Elaborated Pressure Transient Analysis. *Rock Mechanics and Rock Engineering*, **55,** (2022),1931–1954.

Brudy, M., and Zoback, M.: Compressive and tensile failure of boreholes arbitrarily inclined to principal stress axes: Application to the KTB boreholes, Germany, *International Journal of Rock Mechanics and Mining Sciences*, **30(7)**, (1993), 1035–1038.

Carrera, J., and Neuman, S.: Estimation of aquifer parameters under transient and steady state conditions: 2. Uniqueness, stability, and solution algorithms, *Water Resources Research Journal*, **22**, (1986), 211–227.

Carrera, J., Alcolea, A., Medina, A., Hidalgo, J., and Slooten L.J.: Inverse problem in hydrogeology. Hydrogeology Journal, **13**, (2005), 206–222.

Dahrabou, A., Valle, B., Meier, P., Brunner, Ph., and Alcolea A.: A systematic methodology to calibrate wellbore failure models, estimate the in-situ stress tensor and evaluate wellbore cross-sectional geometry, *International Journal of Rock Mechanics and Mining Sciences*, **149**, (2022), 104935.

Deichmann, N., Giardini, D.: Earthquakes induced by the stimulation of an enhanced geothermal system below Basel (Switzerland), *Seismological Research Letters*, **80(5)**, (2009), 784–798.

Doherty, J.: Ground water model calibration using pilot points and regularization. *Ground Water*, **41**, (2003), 170–177.

Doherty, J.: Calibration and Uncertainty Analysis for Complex Environmental Models. Blurb, Incorporated, (2015), ISBN: 978-0-09943786-0-6.

Edwards, A.W.: The history of likelihood, *International Statistical Review*, (1974), 9–15.

Evans, K., Meier, P.: Hydrojacking and hydrofracturing tests in a fissile schist in South-west Switzerland: In-situ stress characterisation in difficult rock, *Proceedings*, Conf. on the Mechanics of Jointed and Faulted Rock, Ed, H.P. Rossmanith, Vienna, Austria (1995).

Guglielmi, Y., McClure, M., Burghardt, J., Morris, J. P., Doe, T., Fu, P., Knox, H., Vermeul, V., Kneafsey, T. and the EGS Collab Team: Estimating Stress from Fracture Injection Tests: Comparing Pressure Transient Interpretations with In-Situ Strain Measurements, *Proceedings*, 47th Workshop on Geothermal Reservoir Engineering, Stanford University, Stanford, California, USA (2022).

Häring, M.O., Schanz, U., Ladner, F., and Dyer, B.: Characterisation of the Basel 1 enhanced geothermal system. *Geothermics*, **37(5)**, (2008), 469–495.

Hoek, E.: Practical Rock Engineering, RocScience, http://www.rocscience.com/hoek/PracticalRockEngineering.asp, 2007.

Houston, H.: Low friction and fault weakening revealed by rising sensitivity of tremor to tidal stress, *Nature Geoscience*, **8**, (2015), 409-415.

Kastrup, U., Zoback, M.L., Deichmann, N., Evans, K.F., Giardini, D., and Michael, A.J.: Stress field variations in the Swiss Alps and the northern Alpine foreland derived from inversion of fault plane solutions, *Journal of Geophysical Research: Solid Earth*, 109(B1), (2004).

Kirsch, G.: Die Theorie der Elastizitat und die Bedurfnisse der Festigkeitslehre, *Z Ver Deutscher Ingenieure*, **42**, (1898),797–807

Kraft, T., and Deichmann, N.: High-precision relocation and focal mechanism of the injection-induced seismicity at the Basel EGS, *Geothermics*, **52**, (2014), 59-73.

Kutter, H.K.: Influence of drilling method on borehole breakouts and core disking, *Proceedings*, 7th Gong. Int. Soc. Rock Mech. (ISRM), Aachen, Balkema, Rotterdam, Vol. 3, 1659–1664.

Kwon, S., Xie, L., Park. S., Kim, K.I., Min K.B., Kim, K.Y., Zhuang, L., Choi, J., Kim, H., and Lee, T.J. Characterization of 4.2-km-deep fractured granodiorite cores from Pohang geothermal reservoir, Korea, *Rock Mechanics and Rock Engineering*, **52(3)**, (2019), 771–782.

Lin, W., Yamamoto, K., Ito, H., Masago, H., and Kawamura, Y.: Estimation of minimum principal stress from an extended leak-off test onboard the chikyu drilling vessel and suggestions for future test procedures. *Scientific Drilling*,**6**, (2008), 43–47.

Marquardt, D.W.: An algorithm for least-squares estimation of nonlinear parameters, *The Japan Society for Industrial and Applied Mathematics*, **11(2)**, (1963), 431–441.

Martin, D., Kaiser, P., and Christiansson. R.: Stress, instability and design of underground excavations. *International Journal of Rock Mechanics and Mining Sciences*, **40,** (2003),1027–1047.

Shen, B.: Borehole breakouts and in situ stresses, *Proceedings*, First Southern Hemisphere International Rock Mechanics Symposium, (2008), 407–418.

Terakawa, T., Miller, S., and Deichmann, N.: High fluid pressure and triggered earthquakes in the enhanced geothermal system in Basel, Switzerland, *Journal of Geophysical Research*, **117(B7)**, (2012), B07305

Valley, B., Evans, K.F.: Stress orientation to 5 km depth in the basement below Basel (Switzerland) from borehole failure analysis, *Swiss Journal of Geosciences*, **102(3)**, (2009), 467–480.

Valley, B., Evans, K.F.: Stress magnitudes in the Basel enhanced geothermal system. *International Journal of Rock Mechanics and Mining Sciences*, **118**, (2019),1–20.

Williams, M.K., Valley, B., Alcolea, A., Meier, P., Guglielmi, Y., Soom, F., Dobson, P., and Cook, P.: Inversion of strain data from a novel step-rate injection test for determining the full stress tensor in deep boreholes, Proceedings, 20th Swiss Geoscience Meeting, Lausanne, Switzerland, (2022).

Zabihian, F., Sohrabi, R., Alcolea, A., Meier, P., and Valley, B.: Deriving full stress tensor profile from borehole failure observations. Proceedings, 20th Swiss Geoscience Meeting, Lausanne, Switzerland, (2022).

Zoback, M., Barton, C., Brudy, M., Castillo, D.A., Finkbeiner, T., Grollimund, B. R., Moos, D.B., Peska, P., Ward, C.D., and Wiprut, D.J.: Determination of stress orientation and magnitude in deep wells, *International Journal of Rock Mechanics and Mining Sciences*. *Special issue of the ijrmms: rock stress estimation isrm suggested methods and associated supporting papers*, (2003), 1049–1076

Zoback, M.D.: Reservoir Geomechanics. Cambridge University Press, 2007. http://dx.doi.org/10.1017/CBO9780511586477.